

Atomic oxygen in crystalline Kr and Xe. II. Adiabatic potential energy surfaces

A. V. Danilychev and V. A. Apkarian

Department of Chemistry, University of California, Irvine, California 92717

(Received 8 October 1993; accepted 4 January 1994)

The potential energy surfaces of atomic oxygen, $O(^3P, ^1D, ^1S)$, trapped in crystalline Kr and Xe are developed based on known angularly anisotropic pair interactions. The electrostatic limit, with the neglect of exchange and spin-orbit interactions, is assumed. Using a classical statistical treatment for the simulation of spectra, the surfaces are shown to reproduce the experimental $O(^1S \rightarrow ^1D)$ emissions in substitutional and interstitial sites of crystalline Kr. The surfaces are also in accord with charge transfer emission spectra of O/Xe solids. With lattice relaxation, the Xe- $O(^1D)$ -Xe insertion site becomes the global minimum, and can therefore act as a stable trap site. This is in accord with experimental observations of a third trapping site in Xe. To rationalize the recently reported long-range mobility of O atoms in these solids [A. V. Danilychev and V. A. Apkarian, *J. Chem. Phys.* **99**, 8617 (1993)], the topology of various electronic surfaces are presented. It is shown that the minimum energy paths connecting interstices on the triplet and singlet surfaces are quite different. The triplet path is strongly modulated and proceeds along body diagonals of the unit cell. The singlet path is more gently modulated and proceeds along face diagonals. These features are consistent with the postulated thermal mobility as proceeding via triplet-singlet conversion. However, on a quantitative basis, the electrostatic surfaces fail to support the model. The site specific crossing energies, including lattice relaxation, are calculated to range between 1.2 and 1.7 eV in Xe and Kr, which is an order of magnitude larger than the observed experimental activation energies of migration. Inclusion of spin-orbit and charge transfer mixing in these surfaces, absent in the present treatment, should reduce this discrepancy.

I. INTRODUCTION

In the paper preceding the present, we reported on experimental studies in crystalline Kr and Xe solids doped with atomic oxygen.¹ The main emphasis of that report was the unusual thermal mobility of O atoms. The experiments, carried out by several techniques, established that O atoms once thermally activated travel several hundred angstroms prior to retrapping. The measurements involved monitoring of O₂ luminescence and laser induced fluorescence from O atoms, either during or subsequent to a temperature ramp. In all cases, it was found that the formation of O₂ proceeds via first order kinetics. Given an initial statistical spatial distribution of atoms, first order recombination implies that the migration range is larger than the average separation between dopants. The required kinetic scheme is illustrated in Fig. 1(a). The initial condition of statistical distribution, necessary for the kinetic argument, is guaranteed by photogenerating O from different precursors, O₂ and N₂O, known to be initially isolated as monomers. The initial distribution is further scrambled in some experiments by extensive irradiation of the atomically doped solids, taking advantage of their photomobility and photothermal mobility. The efficacy of this process is verifiable in solid Kr. The initial photodissociation of N₂O in Kr yields exclusively interstitial O, subsequent irradiation generates substitutional O.¹ The photoinduced mobility of O in Xe matrices has been independently studied, and verified to lead to long-range migration.²

While there is precedent to the observation of photoinduced long-range migration,³ which in the case of F atoms has been observed in molecular dynamics simulations as

well,⁴ the thermally induced process is difficult to rationalize in crystalline solids. We had postulated that the process may be sustained by the specific topology of electronic surfaces of O in heavy rare gas solids.¹ The requisite topology to produce first order recombination is illustrated in Fig. 1(b). Thermal activation leads to access of an electronically excited state, at an energy below the migration barrier on the ground surface. Given that the periodic barriers on the excited state are shallower, the atom may migrate more easily on this surface. To the extent that the migration path on the excited surface avoids the ground surface, the atom may remain mobile until recrossing to the triplet surface. The plausibility of this model is rooted in the *ab initio* pair potentials of O-Kr and O-Xe.⁵ While the ground state $O(^3P)$ -Rg potentials, $^3\Pi$ and $^3\Sigma^-$, are strictly repulsive; the $O(^1D)$ -Rg pair interaction leads to a bound surface, $1^1\Sigma^+$. The $^3\Pi$ and $1^1\Sigma^+$ surfaces cross on the attractive limb of the bound state. Moreover, the equilibrium distance on the excited surface is more than 1 Å shorter than the ground state van der Waals radius.⁵ Thus, while the migration of $O(^3P)$ in crystalline Rg should be subject to large barriers, $O(^1D)$ should fit nicely in the undistorted lattice and may therefore migrate more easily. These same arguments were made in explaining the exciton mediated reversible photodissociation of N₂O in solid Xe, and qualitative surfaces were sketched to explain the extracted kinetics.⁶ In this paper, we attempt to quantify these statements by generating the appropriate electronic surfaces. As a calibration of the constructed surfaces, we use them to simulate the observed emission spectra. The simulations, which rely on a statistical formulation, are in good accord with experiment. The method has also been tested in a re-

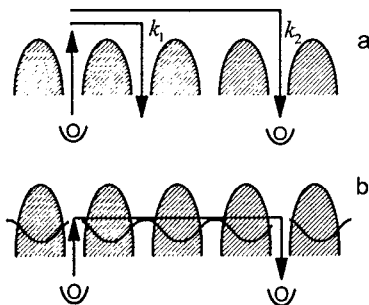


FIG. 1. Models for first order recombination. (a) The trapped O atoms are subject to a periodic potential. Thermal activation may lead to re trapping with a probability of k_1 , or reaction, with a probability of k_2 . First order kinetics is possible only if $k_2 \gg k_1$, i.e., only in the case where the thermally activated atom undergoes long-range migration prior to re trapping. (b) The postulated model involves two electronic surfaces. A crossing between these two surfaces occurs below the barrier top on the ground surface. The periodic potential on the excited state is more softly modulated, and may involve a minimum energy path that significantly avoids the ground state.

lated problem: $I^* \rightarrow I$ emission in solid Kr and Xe.⁷ The Monte Carlo approach adopted here has also been independently implemented by Boatz and Fajardo in their recent simulations of alkali atom excitations in rare gas solids.⁸ The successful reproduction of the known spectroscopy of O/Rg gives confidence to the formulation, and to the constructed potentials at least at stationary, high symmetry sites of the lattice. However, the surfaces fail to yield quantitative agreement for activation energies of thermal migration. This may simply be an indication of the inadequacy of surfaces at short O–Rg distances, where electron exchange cannot be ignored. Among the blatant shortcomings within the model are the neglect of spin–orbit coupling and charge transfer contributions, which are to be expected to be enhanced in the solid state.

In what follows, in Sec. II, we describe the method used for the construction of the many-body potentials, and discuss the approximations involved. In Sec. III, the topologies of the relevant electronic surfaces are described and shown to be in qualitative agreement with the requisite conditions of the postulated migration mechanism. In Sec. IV the spectral simulations are presented and compared to the experimental data. In Sec. V we give the results of Monte Carlo calculations used to evaluate the predicted activation energies by these potentials, which fail to reproduce the experimental values. We close by summarizing implications and delineating possible refinements of the treatment.

II. METHOD

With the exception of S states, the interaction potential of an open shell atom with closed shell rare gas atoms is angularly anisotropic. Accordingly, it cannot be treated in terms of pairwise additive radial functions.⁹ As long as the interactions are dominated by electrostatics, dispersion at long-range and electron–electron repulsion at short range, it should be possible to cast them in terms of angle dependent electrostatic pair potentials.^{9,10} Except for the Rg^+O^- charge transfer admixture, all Rg–O pair potentials can be expected

to be dominated by electrostatics. With this proviso, we proceed with a treatment that retains the minimal rigor necessary for the analysis of adiabatic many-body surfaces. The construction of these surfaces is closely related to those previously presented by Maillard *et al.*, for the crystal field split states of O atoms trapped in high symmetry sites,¹¹ and by Balling and Wright in their treatment of excited states of alkali atoms in rare gas solids.¹² For the consideration of mobility, the description of the entire surface, and in particular unstable points, such as barriers and saddle points connecting stable sites, is required, which is our purpose here. We proceed by considering the interaction Hamiltonian for an oxygen atom in the field of n closed shell rare gas atoms. In first order perturbation, the interaction can be expressed as⁹

$$H_{\text{int}} = V_{O-Rg}(r; R_1, R_2, \dots, R_n) + V_{Rg-Rg}(R_1, R_2, \dots, R_n) \quad (1)$$

in which r and R represent, respectively, the electronic coordinate on the O atom and the coordinates of the rare gas atoms as measured from the origin centered on the oxygen core. Note, O has two valence electrons which are treated as coupled in the atomic limit. The single variable r is used to represent the electronic degree of freedom as an effective charge distribution. Accordingly, we will denote its orbital angular momentum as $l \equiv L = l_1 + l_2$, and $m \equiv M_L$. It is assumed in Eq. (1) that the interactions between O and Rg do not effect Rg–Rg interactions, and both spin–orbit and hyperfine contributions are ignored. The angular dependence of V_{O-Rg} is then expanded in Legendre polynomials, $P_L(\mathbf{r} \cdot \mathbf{R}_k)$:

$$V_{O-Rg}(r; R_1, R_2, \dots, R_n) = \sum_{k=1}^n \sum_{L=0}^{\infty} V_L(r, R_k) P_L(\mathbf{R}_k \cdot \mathbf{r}) \quad (2)$$

and the electronic eigenenergies are obtained by diagonalizing V_{O-Rg} in the uncoupled basis sets, $|lm\rangle_O |ns\rangle_{Rg}$; $l=1$ for $O(^3P)$; $l=2$ for $O(^1D)$. The closed shell rare gas functions, $|ns\rangle_{Rg}$, will be dropped from further explicit notation. Using the addition theorem for the expansion of the Legendre polynomial, H_{int} can be evaluated as the product of spherical harmonics:

$$V_{mm'} = \sum_{k=1}^n \sum_{L=0}^{\infty} \frac{4\pi}{2L+1} \times \langle Y_{lm'}(\vartheta, \varphi) | \sum_{M=-L}^L Y_{LM}(\vartheta, \varphi) | Y_{lm}(\vartheta, \varphi) \rangle \times V_L(R_k) Y_{LM}^*(\vartheta_k, \varphi_k) \quad (3)$$

in which the subscript k refers to the rare gas atoms, of which there are n , the unsubscripted coordinates are for the O atom electron, and L is the order of the Legendre polynomial. The conditions $l+L+l'=\text{even}$, and $l+L+1 \geq 0$, limit the summation over L . Only two terms, $L=0, 2$, contribute in the case of $O(^3P)$, and only three terms, $L=0, 2, 4$, contribute in the case of $O(^1D)$. The individual matrix elements V_{mm} , using the real 1D basis set, are given explicitly in Appendix A.

The required radial functions $V_L(R)$ are extracted from either *ab initio* or experimental pair potentials, using well known relations. In the absence of coupling between 1D and 3P bases, the required relations for the P state are¹³

$$V_0 = \frac{1}{3}(V_\Sigma + 2V_\Pi); \quad V_2 = \frac{5}{3}(V_\Sigma - V_\Pi), \quad (4)$$

while for the D state, they are

$$V_0 = \frac{1}{5}(V_\Sigma + V_\Pi + V_\Delta),$$

$$V_2 = (V_\Sigma - V_\Delta) + (V_\Pi - V_\Delta), \quad (5)$$

$$V_4 = \frac{9}{5}(V_\Sigma - V_\Pi) + \frac{3}{5}(V_\Delta - V_\Pi).$$

The ground state potentials, $^3\Pi$ and $^3\Sigma^-$ required in Eq. (4), are available from molecular beam scattering data.¹⁴ They are used to treat the many-body surfaces of $O(^3P)$ without further modification. The required pair potentials for the 1D states are taken from *ab initio* data which are given with a stated accuracy of 0.05 eV.⁵ Since these do not include long-range dispersion, a C_6/R^6 contribution weighted by the Buckingham–Corner damping function, $\zeta(R)$, is added:

$$V_{\text{disp}} = \zeta(R) \frac{C_6}{R^6} \begin{cases} \zeta(R) = \exp\left[-4\left(1 - \frac{R_m}{R}\right)^3\right] \\ \quad \text{for } R_m > R \\ \zeta(R) = 1 \quad \text{for } R_m < R \end{cases}. \quad (6)$$

This procedure follows that of Maillard *et al.*,¹¹ except in our case the dispersion term is limited to only R^{-6} . R_m is chosen to coincide with the experimental potential minimum on the ground state, and the same value is used for all states ($R_m = 3.75 \text{ \AA}$ for O–Kr).¹⁴ The C_6 values for V_L were extracted, using the relations of Eqs. (4) and (5), from recommended state specific pair interaction parameters.^{15,16} Due to the difference relations in Eq. (5), and the similarity in diatomic C_6 terms, the long-range correction to V_4 is negligible (it is much smaller than the uncertainties in difference potentials). For computational purposes, it is useful to represent the different potentials in relatively simple analytical forms. Such fits are possible within stated accuracies of the *ab initio* data. As expected for $e-e$ repulsion, combinations of Gaussians and exponentials are quite adequate for these curves. The explicit functional forms and parameters used in the simulations are given in Appendix B, along with a comparison with the *ab initio* points.

The Rg–Rg interactions are assumed to be pairwise additive radial functions. The Barker–Fisher–Watts pair potential is used for $V(\text{Rg–Rg})$.¹⁷

The potential energy surfaces are evaluated for all states, for a given configuration of the doped lattice. The 1S surface is a simply additive function of the atomic coordinates. For the states arising from the 3P and 1D basis, the matrix elements of Eq. (3) are summed over all rare gas atoms, the matrices— 3×3 for the 3P basis and 5×5 for the 1D basis—are then diagonalized and all eigenvalues obtained.

Prior to proceeding with the description of the resulting surfaces, we note the main approximations made above. Firstly, it should be noted that Eq. (3) is identical to the electrostatic expansion of a nonpolarizable charge distribution in an electric field.¹⁸ This is equivalent to limiting the

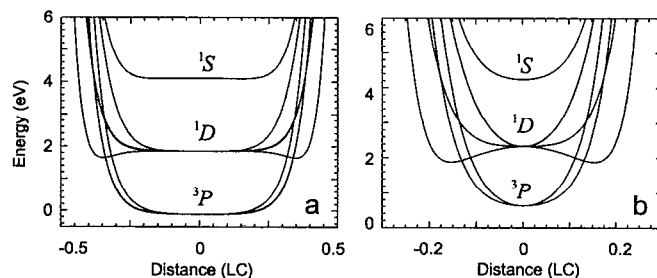


FIG. 2. Crystal field split potentials of O/Kr; (a) Substitutional O_h ; (b) interstitial O_h site. The abscissa is for translation of the O atom along the line joining two Kr atoms, and is given in units of the lattice constant.

interaction potential to two-body terms, i.e., the charge distributions on neither O nor Rg atoms are polarized by their mutual interactions. The treatment does not include three-body or higher order terms. The treatment makes the implicit assumption that the two-body potentials obtained from gas phase scattering experiments are transferable to the many-body system by the simple decomposition of Eqs. (4) and (5). Consistent with this scheme, no mixing between singlet and triplet manifolds is assumed in the diabatic basis. The calculations are accordingly restricted to spatial coordinates, in a strictly $|LM\rangle$ basis set, despite the fact that these are not conserved quantities. In the more appropriate coupled representation, $|Jm_j\rangle$, mixing between 1D and 3P surfaces will occur through spin–orbit coupling. In the pair potentials, these interactions have been considered in some detail, since they are responsible for the quenching of $O(^1D)$ atoms by collisions with rare gases.^{15,19} At the crossing points, $V_{s.o.} = \langle ^3\Pi | H_{s.o.} | ^1\Sigma^+ \rangle = 500 \text{ cm}^{-1}$ for XeO, and 200 cm^{-1} for KrO.¹⁵ The origin of these couplings is understood in terms of the charge transfer admixture at these configurations, and the large spin–orbit splittings in Rg^+ . With the solvation of ionic states in these polarizable solids, larger charge transfer contributions are to be expected and accordingly stronger coupling of these states should result. Quite clearly, for thermal dynamics at the cryogenic temperatures of the present studies, the crossings arising from $m_j = 0$ components should be strictly avoided, i.e., the triplet and singlet configurations are directly connected on the adiabatic surfaces.

III. RIGID LATTICE POTENTIAL ENERGY SURFACES

The potential energy curves for an O atom trapped in interstitial and substitutional octahedral sites in Kr, are shown in Fig. 2, for motion along a line containing rare gas atoms at each end (e.g., along $[1,0,0]$ in the interstitial O_h site, and along $[1,1,0]$ in the substitutional O_h site). These curves can be directly compared to those previously published by Maillard *et al.*¹¹ They are quite similar in their qualitative features. To inspect the rigid lattice surfaces, potential energies were evaluated on a grid of $50 \times 50 \times 50$ points, spanning a full octant of the unit cell. The cube was then inspected slice by slice, to ensure that all crossings, saddle points, and extrema were identified. Only the most relevant slices are shown here. The origin of the energy is taken as that of a free O atom and undoped lattice at its

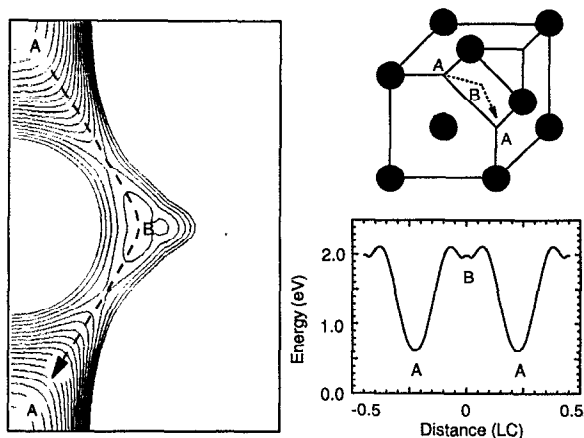


FIG. 3. The minimum energy surface of the diabatic 3P potential connects two octahedral interstitial sites through the T_d center. A surface of section that contains the minimum energy path, is shown on the unit cell. The contour lines are spaced by 0.1 eV. The minimum energy path connecting two interstitial O_h sites is also shown.

equilibrium geometry. Two-dimensional surfaces, that contain two interstitial sites and the minimum energy path for a given state, are illustrated in Figs. 3 and 4. In Fig. 3 the lowest surface arising from the 3P eigenstates is shown. In Fig. 4, the lowest potential energy surface of the system is shown. The latter is equivalent to assuming avoided crossings between the lowest of 1D and the lowest of the 3P eigenstates. In the absence of inclusion of spin-orbit coupling, this surface can be regarded as the adiabatic minimum energy surface that controls thermal dynamics.

The potential minima, and minimum energy paths between minima, are quite different for the two surfaces shown in Figs. 3 and 4. The 3P surface is characterized by repulsive interactions, accordingly the global minima on this surface are found at the O_h interstitial sites, which represent the largest cavities. The minimum energy path between two such

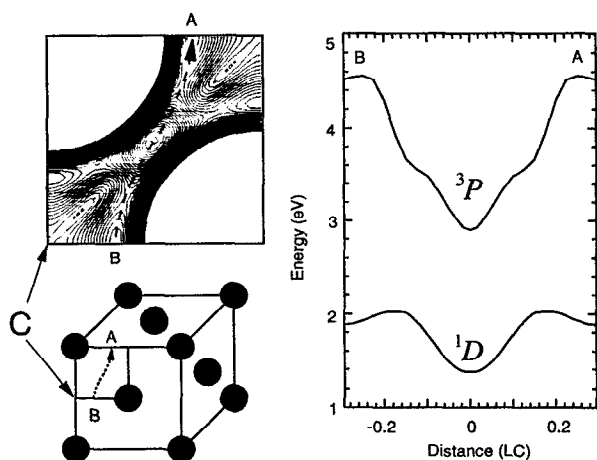


FIG. 4. The adiabatic minimum energy surface connecting O_h interstitials in Kr occurs on the unit cell faces. The minimum energy path, which avoids the 3P minima is also shown. Along the indicated path, the 3P potential remains >1 eV above that of the 1D , as indicated by the potential energy curves vs travel distance.

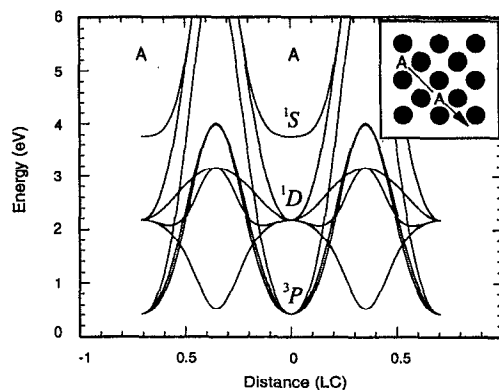


FIG. 5. Potential energy curves in Xe connecting the O_h interstitial to the Xe-O-Xe insertion sites. The 1D minima that occur at the insertion sites are only 0.15 eV higher than the 3P minima that occur at the center of the octahedron.

cavities can be located on the $(\frac{2}{3}, 0, \frac{2}{3})$ plane, as indicated in Fig. 3; it involves an $O_h-T_d-O_h$ path. The potential curve along this minimum energy path is also shown. Entrance and exit of the T_d site proceeds on a D_3 axes perpendicular to the faces of the tetrahedron, with a 70° angle of deflection connecting them near the body center. The potential minimum which occurs at the interstitial O_h site is at 0.62 eV in Kr and at 0.42 eV in Xe. The minima are separated by barriers of 1.47 eV in Kr and 1.23 eV in Xe.

The topology of the minimum energy surface in Fig. 4 is dominated by the 1D configuration, except for the deep interstitial O_h minima, which are leftover from the 3P configuration of Fig. 3. The 1D surface is characterized by attractive interactions. Accordingly, the potential minima appear in the tightest sites, namely, between two Rg atoms. In effect, a linear triatomic is formed at an energy of 1.37 eV in Kr and 0.53 eV in Xe. The latter is only 0.11 eV higher than the global minimum, i.e., the 3P interstitial O_h site. Thus, if we consider the avoided nature of crossings between the lowest of 3P and 1D surfaces, an effective halving of the periodicity of the potential for travel along face diagonals results. This is illustrated in Fig. 5 for the case of O/Xe, for travel along $[2,0,2]$ direction. Note, the 1D energy of the free atom is 1.97 eV, therefore the binding energies in these Rg- $O(^1D)$ -Rg insertion configurations correspond to 0.95 eV in Kr, and 1.61 eV in Xe. We will return to the reliability of these minima below. The minimum energy path connecting purely 1D minima is also on the faces of the unit cell, e.g., on the $(1,0,0)$ plane as indicated in Fig. 4. The barrier connecting the minima is at 0.66 eV in Kr and 0.82 eV in Xe. The path correspond to an oscillating motion along the $[2,0,0]$ direction, involving only a small angle of deflection, 20° , as indicated on the surface in Fig. 4. Such a travel is only possible if the trajectory is retained from falling in the 3P minimum, which appears as the lowest minimum in the surface of Fig. 4. The retaining barrier is ~ 0.3 eV in the case of Kr.

The qualitative ingredients sought to explain the observed long-range migration are realized with the constructed surfaces. These are the following.

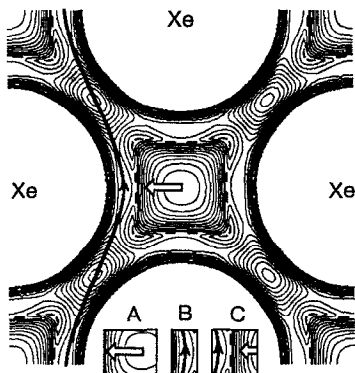


FIG. 6. The adiabatic minimum energy surface in Xe, showing the suggested paths of (a) activation, from the 3P interstitial O_h minimum to the nearest 1D crossing; (b) migration path on the 1D surface; (c) the barrier for retrapping. The contour lines are spaced by 0.1 eV.

(i) The trajectories of migration on the 3P and 1D surfaces are along two different paths.

(ii) Migration on the excited singlet surface involves a periodic barrier less than half as large as the barrier on the triplet ground surface.

(iii) Moreover, the minimum energy path on the triplet surface is strongly curved, therefore it can only be navigated with near head-on collisions resulting in large momentum and energy exchange, while the migration path on the singlet surface requires near grazing collisions and therefore little momentum exchange. Thus, retrapping should be efficient on the 3P surface, and diffusive mobility should be expected. On the difference surface, or on the 1D surface, it can be imagined that cooperation with lattice phonons to generate small deflections can lead to long-range motion without significant retrapping. Such a trajectory was previously found in the impulsive photodissociation induced migration of F atoms.⁴ There, only radial pair potentials were assumed in the simulations. A proper treatment of this dynamics should include the electronic angular momentum, which should yield profoundly different dynamics due to Coriolis forces. It can, for instance, be expected that curved paths may be navigated with substantially reduced momentum exchange.

The surface in Fig. 4 makes it clear that for an interstitial O atom to undergo long-range migration via this minimum energy surface, it would have to be activated from the O_h trap site onto the 1D region, and would have to migrate on a narrow trail to avoid retrapping. The expected paths are presented in Fig. 6 for the case of O/Xe. The narrow ridge, which separates the migration path from the interstitial O_h site, should be sensitive to the extent of spin-orbit coupling. The activation energies for this process in the rigid lattice should be given by the energy barrier separating the O_h interstitial minimum from the nearest migration ridge, these are 1.4 eV in Kr and 1.1 eV in Xe.

To this point, we have considered that the atoms are trapped on the 3P surface, and once activated to the 1D surface they migrate on it, until recrossing. Part of the attractiveness of this model is the fact that it provides for a long-

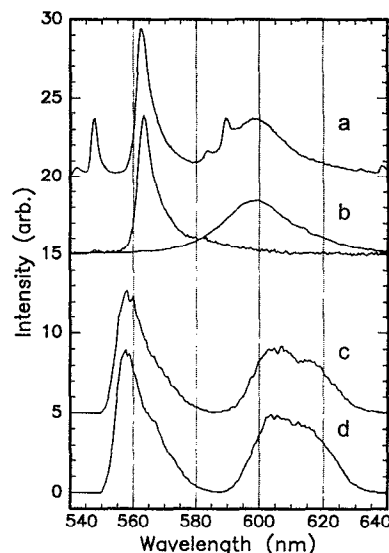


FIG. 7. Comparison between experimental and simulated spectra for O/Kr. The interstitial and substitutional site emissions occur at 599 nm, and 563 nm, respectively: (a) experimental spectrum obtained from the photodissociation of O_2 in Kr (the sharp lines, which occur as pairs, are O_2 emissions, for details see Ref. 1); (b) experimental spectra obtained after photodissociation of N_2O in Kr, the atomic emissions in the two different sites are separated by thermal cycles; (c) simulated spectrum assuming electric quadrupole transitions; (d) simulated spectrum assuming cage anisotropy induced transitions.

range migration mechanism without invoking coherent dynamics between the impurity and lattice phonons. Nevertheless, Fig. 5 suggests a different possibility, at least in the case of Xe. Firstly, given the similarity of the 1D and 3P minima, the atom may be trapped in either. Secondly, and if we include spin-orbit splitting, it is clear that the indicated migration path corresponds to the one with the lowest amplitude of energy modulation (~ 1.2 eV), and highest frequency of modulation. It however passes through successive $^3P-^1D-^3P$ minima, which corresponds to passage through sites of local symmetry $O_h-D_{\infty h}-O_h$. Therefore, the only possible mechanism for long-range migration along this path is coherent coupling of the atom to long-wave phonons, and band-type motion. Despite the halving of the modulation period, in the present surfaces, the barriers seem too large to sustain such a transport mechanism.

IV. SIMULATION OF ATOMIC SPECTRA

A partial test of the reliability of the constructed surfaces comes from their ability to reproduce the observed experimental spectra. The case of O/Kr is particularly useful, since two emission bands are observed and assigned to $O(^1S) \rightarrow (^1D)$ in two different sites. The experimental spectra are shown in Fig. 7. The 563 nm band is assigned to emission in the substitutional site, while the 599 nm band is assigned to the interstitial site. These assignments are based on photogeneration histories, thermal histories, and radiative lifetimes of the two bands.¹

We proceed with a strictly classical statistical simulation. The treatment is justified with the realization that although at

cryogenic temperatures, the system can be regarded to be in the high temperature limit with respect to lattice vibrations.²⁰ More specifically, the variation of the adiabatic potentials within the average de Broglie wavelength of atomic motion $\hbar(\beta/\mu)^{1/2}$ is small compared to the thermal energy $1/\beta[\beta=(k_B T)^{-1}]$:

$$\beta \left(\frac{\hbar}{(\mu k_B T)^{1/2}} \nabla_{\{R_i\}} V_I \right) < 1. \quad (7)$$

This condition can rigorously be verified for each surface by evaluating the expectation value of the force matrix for each eigenstate, J :

$$|\nabla_{\{R_i\}} V_I| = \left[\sum_i \left(\langle I | \frac{\partial}{\partial R_i} V_{\text{int}} | I \rangle \right)^2 \right]^{1/2}. \quad (8)$$

The classical multidimensional reflection approximation is then used to evaluate emission line shapes:²⁰⁻²²

$$I(\omega) \propto Z^{-1} \omega^3 \int \frac{e^{-\beta V_i(R_1, R_2, \dots, R_n)} |\mu_{if}|^2 \delta_R[(V_f - V_i)/\hbar - \omega] \Pi_j dR_j}{|\nabla_{\{R_j\}}(V_f - V_i)|} \quad (9)$$

in which the delta function emphasizes that according to the Franck principle the optical transitions involve changes in potential energies alone, which are explicit functions of all lattice coordinates: $V(r; R_1, R_2, \dots, R_n)$. Moreover, it has been indicated that the delta function is properly normalized in coordinate space, since it occurs inside the integral over coordinates. The denominator, the gradient of the difference potential, represents the density of states and arises from the transformation of the delta function from energy to coordinate space.²² Although the denominator is included in Eq. (9) for the sake of completeness, its effect is relatively minor on the final results, and its evaluation is rather tedious.⁷ We have therefore ignored this term in the results to be shown. This approximation is formally equivalent to the assumption of constant density of states, which is, in part, justified by the condition of Eq. (7). Here, the initial state is the 1S surface, which is a function of rare gas coordinates alone, as indicated in the Boltzmann factor. The integration is over all lattice coordinates, and Z is the classical partition function—the transitions are a weighted average over all initial configurations of the system. The ω^3 factor arises in emission due to the summation over final photon states.²¹ The final states of interest here are the five surfaces that arise from the $O(^1D)$ configuration. The electronic transition moment, μ_{if} , is evaluated by two different methods. Noting that in the atomic basis set the $^1S \rightarrow ^1D$ transition is allowed via electric quadrupole, and that the quadrupolar charge distribution would be the expected leading term in the high symmetry trapping sites that are considered, we make the Condon approximation, i.e., assume a transition probability independent of the lattice configurations. Electric quadrupolar transitions to all five surfaces are equally probable in this case, accordingly, the spectrum is generated by summing Eq. (9) over all five final eigenstates. An approximate treatment of electric dipole transitions induced by the cage anisotropy was also implemented (see Appendix C). In this approach, the first moment of the cage anisotropy is computed for a given configuration and transitions to the different surfaces weighted accordingly.

The implied spectral distribution by Eq. (9) is most conveniently evaluated by Monte Carlo methods. The upper state can be treated as strictly pairwise additive, and a stan-

dard Metropolis algorithm is used to generate the properly weighted initial state configurations.²³ For every new configuration of the system, the interaction Hamiltonian is diagonalized to evaluate the terminus eigenstates. A histogram of the transition energies summed over all five eigenstates constitutes the spectral distribution. Initially 108 atoms were used with periodic boundary conditions for the simulations. It was, however, discovered that the derived spectral simulations were quite comparable to those in which only two nearest neighbor shells were allowed to move while the rest of the lattice was held rigid—the surfaces are determined by mostly short range interactions. The resulting spectra for interstitial and substitutional O/Kr are shown in Fig. 7, using electric quadrupole (trace *c*) or anisotropy induced dipole (trace *d*) for the transition probabilities. There is little difference between the two simulated spectra. The similarity is the result of the fact that on average, the trapped O atom experiences a cage of octahedral symmetry. Accordingly, the first moment of the cage anisotropy averages out and the second moment is equivalent to a quadrupolar charge distribution.

The comparison between experimental and simulated spectra of Fig. 7 is quite acceptable. The features to compare include the absolute energies of the bands, the separation between interstitial and substitutional band centers, and the widths and asymmetries of the individual bands, i.e., at least three moments of the spectral distribution for each of the bands are satisfactorily reproduced. In the interstitial site, the simulation shows a broader peak due to an exaggerated splitting between the T_{2g} and E_g states. To test the sensitivity of the spectral features to pair interaction parameters, we have varied the dispersion contributions. A change of 20% in the C_6 coefficient of the 1S state yields a spectral shift of 20 nm. It is therefore clear that adjustment of parameters within the range of the errors of *ab initio* potentials, or the added dispersion term, can lead to a more exact agreement. Such a refinement is not necessary for our present aims. The simulations validate (a) the experimental assignment of the sites, (b) that the constructed potentials in the case of O/Kr, at least near the trap site center, are quite reliable, and (c) the statistical approach to spectral simulations among multiple electronic states is quite successful. It is also possible to extract from the simulations information about the extent of lattice

relaxation around $O(^1S)$. In the interstitial octahedral site of Kr, the atom remains symmetrically trapped, the cage expands radially—the first nearest neighbors move out by 0.17 Å, while the second nearest neighbors move in by 0.01 Å. In the substitutional site, the atom traps asymmetrically, in shallow, thermally accessible C_4 pockets. This is the main origin of the emission line shape of a sharp blue edge and a long red tail from this site. The cage distortions are minor in this case. We note that without the proper thermal relaxation of the lattice, neither the spectral shapes, nor the spectral positions can be predicted. This is the main origin of the difference between the predictions of Maillard *et al.*¹¹ and the present simulations.

The reliability of the deeply bound section of the 1D surface is more relevant to the mobility of atoms. This portion of the potential is not interrogated experimentally in the case of O/Kr, however, it is believed to be accessed in the case of O/Xe in which the emitting state is assigned to the Xe^+O^- .²⁴ The charge transfer emission spectra in Xe were reported and analyzed previously in terms of one dimensional potentials. Based on Franck–Condon analyses of the 370 nm band, it was established that the ionic upper state is aligned with the minimum of the 1D surface, which was estimated to be bound by 1.5 eV. Moreover, it was established that the local minimum of the terminus potential is nearly harmonic, sustaining an O atom frequency of 360 cm^{-1} .²⁴ As discussed in Sec. III, the minimum on the 1D surface occurs in the Xe–O–Xe insertion site. In the unrelaxed lattice, the binding in this site is 1.64 eV according to the present surfaces (see Fig. 5). From the curvature of the potential along the Xe–O–Xe coordinate, and perpendicular to it, harmonic frequencies of 440 and 255 cm^{-1} are obtained. Thus, the global minimum on the present 1D surface, is quite consistent with the earlier spectroscopic analysis of the charge transfer emission spectrum. This conclusion should be qualified. In O/Xe, two emission bands are observed with identical radiative lifetimes, one at 750 nm, and another at 370 nm. In the diatomic framework, these were assigned to $Xe^+O^-(3^1\Sigma^+) \rightarrow XeO(^1\Pi)$ and $(1^1\Sigma)$, respectively. In the present surfaces, if the upper state is located 3.35 eV (370 nm) vertically above the 1D minimum, all other transitions occur in the IR, and no transitions at 750 nm are possible. This may simply reinforce the notion that in the tight sites the repulsion on the unbound 1D states ($^1\Pi$ surface in particular) is overestimated. We also note that, emission at 750 nm is possible for asymmetric trapping in the interstitial O_h site. As long as the charge transfer state is a tight localized diatomic configuration, which was argued to be the case,²⁴ then emissions are not limited to high symmetry sites of the lattice. As long as the internuclear separation in Xe^+O^- is comparable to the Xe–O separation in the insertion site, this part of the 1D surface will be sampled. Thus, the absence of an independent check on the energy of the emitting state, makes the knowledge of the binding on the 1D surface less certain. Finally, we note that in the thermoluminescence measurements in Ref. 1, while only two glow peaks are observed in Kr, three peaks are observed in Xe. The two peaks in Kr could be directly assigned to activation of interstitial and substitutional O atoms. The same two as-

signments are undoubtedly operational in the case of Xe as well. Given the similarity in energy of the 1D and 3P minima in Xe, quite clearly when lattice relaxation is allowed around either site then it becomes the global minimum for interstitial trapping. Thus, the Xe–O(1D)–Xe insertion site provides a rationale for the third site in Xe and its absence in Kr. This consideration, and the agreement with the prior spectroscopic analyses, leads us to conclude that the computed insertion site binding is in relatively good agreement with experiment.

These concerns are, in part, due to the fact that the potential in the tight insertion site, is the least justifiable in the present construct. Due to lowering of ionic states by solvation, we would have expected a larger admixture of charge transfer character here, as compared to the gas phase $1^1\Sigma^+$ pair potential. An increase in ionic character of the lower state, in the form of a Coulombic contribution, of the order of few percent renders the 1D minimum as the global minimum, i.e., it will be stabilized below the 3P surface. This would lead to predominant trapping of O atoms in the triatomic Xe–O–Xe configuration as singlet ground states. This consideration should be made with some care, if we consider the ionic admixture in the insertion site to be that of

$$\alpha|Xe-O-Xe\rangle + \beta(|Xe^+O^-Xe\rangle + |XeO^-Xe^+\rangle),$$

then, in addition to the lowering of the ionic states by solvation, the repulsion between O^- and Xe should be taken into account. Given the tight nature of the site in question, the latter term may be comparable to the ion-pair solvation energy (estimated in Ref. 24 to be ~ 0.75 eV). A similar insertion geometry arises in the case of halogen atoms in rare gas solids when the angularly anisotropic potentials are taken into account.²⁵ There, it has been argued that the consideration of the purely covalent pair interactions leads to an overestimate of the binding in the insertion site, while a more systematic treatment of the ionic admixture via DIM type calculations,²⁶ lead to a smaller stabilization. Our aim here is to establish the extent of the utility of the electrostatic surfaces, notwithstanding the fact that they can clearly be refined by many reasonable considerations. We should also note that Maillard *et al.*, have rejected the formation of this binding site as “chemical nonsense,” and introduced a three-body term in their potentials to eliminate the possibility of linear triatomic σ bonding.¹¹ Their rejection would have been justified had the binding in $XeO(1^1\Sigma^+)$ been of truly chemical nature, however, since this interaction is characterized by electrostatics and partial charge admixture, we may expect it scale in many-body media close to full additivity.

Within the uncertainties of the pair potentials, the relatively simple construct of the many-body surfaces are in surprisingly good agreement with the available spectroscopy in these systems. We therefore surmise that the topology of these surfaces, should, at least qualitatively, explain the observed long-range migration.

V. ACTIVATION ENERGIES

The fundamental quantities extracted from the experimental first order recombination rates are the activation energies and their associated frequency factors. These rate con-

TABLE I. Energetics of trap sites, and $^3P-^1D$ crossings, and effect of lattice relaxation.

	Kr		Xe	
	Interst. O_h	Subst. O_h	Interst. O_h	Subst. O_h
3P barrier height (eV)		1.48		1.28
1D barrier height (eV)		0.65		0.98
Rg-O-Rg binding (eV)		0.96		1.64
$^3P \rightarrow ^1D$, unrelaxed (eV)	1.40	1.77	1.09	1.66
$^3P \rightarrow ^1D$, relaxed (eV) ^a	1.67	1.77	1.29	1.66
Relaxation energy of crossing (eV)	0.15	~0.01	0.08	~0.01
3P min., unrelaxed (eV)	0.63	-0.12	0.42	-0.13
3P min. relaxation (eV)	0.42	~0.01	0.28	~0.01

^aDifference in energy between fully relaxed energy of the trap site, and the fully relaxed energy of the crossing between 1D and 3P surfaces.

stants describe the thermal probability of raising the O atom from an initially stable trapped state unto a mobile state. Site dependent activation energies ranging between 0.05 and 0.13 eV, and frequency factors ranging from 10^7 to 10^{12} s⁻¹ were extracted from the kinetic analysis. According to our postulated model, and in the present surfaces, this should correspond to thermally accessing the crossing between the singlet and triplet surfaces. The desired quantities are free energies, which include lattice relaxation. Although the calculations are limited to a constant V, T ensemble, we expect that the differences between relaxed energies of different sites and the associated minimized crossing energies are a good representation of the true activation energies.

The calculation of lattice relaxation contributions to the energies of the stable trap sites is direct. This is achieved by placing the O atom initially in the unrelaxed lattice, and subsequently carrying out a Monte Carlo simulation at a fixed temperature, 20 K, allowing all atoms to move. For each configuration of the lattice, the interaction Hamiltonian is evaluated and diagonalized to compute the eigenenergies. The acceptance decision of a given configuration is made based on the difference between the lowest eigenvalues. This is tantamount to assuming that the electronic degree of freedom on the O atom is much faster than the lattice motions, i.e., equivalent to *adiabatic following*. The energies of different sites with and without lattice relaxation are tabulated in Table I. Note, in the tight interstitial O_h sites significant relaxation occurs, while in the substitutional sites the relaxation energies are negligible. It is also interesting to note that in the Xe-O-Xe insertion site on the 1D surface, the relaxed energy of the trap is deeper than that of the O_h interstitial site on the 3P surface.

To find the minimum crossing energies a constrained Monte Carlo search is conducted. This is achieved by initially placing the O atom at the crossing of the unrelaxed lattice. The temperature of the system is then artificially raised, and a Monte Carlo walk is conducted in which in addition to the standard Boltzmann weighted acceptance condition for stepping among configurations, we demand that the two surfaces remain within a specified energy, Δ . The temperature of the system is then reduced gradually, usually when a local minimum is reached. The lowest of these crossing energies is then compared to the relaxed energies in different trap sites. This search did not produce

configurations significantly different than those found on the unrelaxed surfaces. In effect, the minimum energy of crossing between 1D and 3P surfaces is dictated mainly by a single pair interaction. The energies of the crossings, with and without lattice relaxation are also included in Table I. In Kr, the lowest crossing is found to be 1.67 eV above the relaxed interstitial site energy, and 1.2 eV above the relaxed substitutional site energy. In Xe the crossing occurs at 1.09 eV above the interstitial O_h site, 1.66 eV above the substitutional O_h , and 1.18 eV above the insertion site. These values are an order of magnitude larger than the experimental activation energies. Quite clearly, on a quantitative basis the present surfaces do not yield a direct interpretation of the observed activation energies for long-range migration of atomic oxygen in these solids.

VI. CONCLUSIONS

The dynamics of open shell systems, atoms, or molecular radicals is dictated by anisotropic pair interactions. The topology of resulting surfaces in condensed media, even in the absence of many-body terms, can vary dramatically depending on the details of the electronic configuration. Such surfaces control the dynamics of the system, be it thermal and adiabatic or sudden as in the case of photoinduced processes. While these seem obvious considerations, they have all but been neglected in past treatments of molecular dynamics in these model systems. The exception being, to our knowledge, the recent treatment of Gersonde and Gabriel aimed at including nonadiabatic dynamics in the solid state.²⁵ Atomic oxygen, trapped in rare gas solids, is a useful model for the investigation of implications of multiple, degenerate electronic configurations. We have presented the surfaces relevant for adiabatic dynamics, in an effort to rationalize the recently observed, thermally induced, long-range migration of O in crystalline Kr and Xe.¹ The treatment, although far from being complete, highlights the dramatic differences in surfaces, and accordingly in dynamics, to be expected from a 1D vs 3P atom. Among the noted differences are (a) the potential minima on the 3P surface correspond to the largest cavities, while those on the 1D surface correspond to the tightest insertion sites of the solid; (b) the potential barrier along minimum energy paths connecting sites is over 2 eV on the 3P surface, while only ~0.7

eV on the 1D surface (in Kr); (c) the minimum energy path on the 3P surface is along body diagonals, while those on the 1D surface is along face diagonals of the unit cell. These differences explain some of the previously documented photodynamics relating to atomic oxygen in rare gas solids. The photodissociation of N_2O which proceeds via $N_2+O(^1D)$ has nearly unit quantum yield, while the predissociation of $O_2(B)$ which produces $O(^3P)+O(^3P)$ is extremely inefficient.^{1,2} O atoms photogenerated by photodissociation of N_2O are subject to long-range migration.² Photomobility has also been documented for O atoms when excited via the Rg^+O^- charge transfer states.²³ In both cases the optical excitation leads to formation of $O(^1D)$. All of these observations are in accord with the differences in 1D vs 3P surfaces, the most common characteristic of these surfaces being that effectively $O(^1D)$ is smaller than $O(^3P)$. Our main interest has been the curious thermal mobility of O atoms trapped in Kr and Xe, in which we have documented that the migration involves a range of order of 100 Å.¹ Such a migration, at temperatures ranging between 20 and 50 K, seems impossible when considering the $O(^3P)$ electronic surface. We had therefore postulated a mechanism involving thermally induced triplet-singlet conversion, and subsequent migration on the 1D surface until recrossing. Although the presented surfaces fail to reproduce the observed activation energies, they are generally consistent with the proposed model. They also reproduce the observed spectroscopy of O atoms in Kr, and the experimental observation of two trap sites in Kr and three trap sites in Xe.¹ The failure to reproduce the activation energies may be related to the neglect of spin-orbit mixing in the present treatment. Higher order perturbations, including increased charge transfer admixture in these surfaces, should also bring down the crossing between singlet and triplet surfaces, and should be considered in a more refined treatment. It is also important to note that once activated, the mechanism that leads to long-range migration is not trivially obvious. Past treatments of this process have used strictly isotropic potentials.⁴ A very different dynamics should result when electronic angular momentum of open shell atoms is taken into consideration. We would expect Coriolis forces to come into play, which may enable the nuclear trajectories to bend around corners that have to be navigated, with little energy exchange between the mobile atom and those of the lattice. These mechanics, coupled with long wave lattice phonons, may hold the key to understanding the long-range migration dynamics of open shell atoms in these media.

We have implemented an approximate, classical statistical treatment of the spectroscopy of atomic electronic transitions using Monte Carlo methods. The treatment is highly successful in reproducing the site specific spectra of $O(^1S)$ in crystalline Kr. The success of the treatment here, and in a related system ($I^* \rightarrow I$ transition in Kr and Xe) (Ref. 7) is taken as justification of the approach. Moreover, it shows that the anisotropic pair interactions, in the electrostatic limit, are a good representation of the potential energy of the many-body system at least at high symmetry points of the lattice. The implementation of the method is direct, and should be generally applicable to electronic transitions in many-body media.

ACKNOWLEDGMENTS

This research was supported by the U.S. Air Force Phillips Laboratory under Contract No. S04611-90-K-0035; and in part by the University of California Irvine through an allocation of computer resources.

APPENDIX A: MATRIX ELEMENTS FOR THE INTERACTION HAMILTONIAN IN THE D BASIS SET

The explicit $V_{mm'}$ matrix elements for the p basis set ($l=1$), have been given in polar coordinates by Balling and Wright,¹² with an algebraic error that has been corrected in the manuscript by Boatz and Fajardo.⁷ For computational purposes, we find it most convenient to use Cartesian coordinates, in a real basis set. For the real D basis set

$$\begin{aligned} |1\rangle &= Y_{2,0}, \\ |2\rangle &= (1/\sqrt{2})(Y_{2,2}+Y_{2,-2}), \\ |3\rangle &= (i/\sqrt{2})(-Y_{2,2}+Y_{2,-2}), \\ |4\rangle &= (i/\sqrt{2})(Y_{2,1}+Y_{2,-1}), \\ |5\rangle &= (1/\sqrt{2})(-Y_{2,1}+Y_{2,-1}), \end{aligned} \quad (A1)$$

the interaction matrix \mathbf{V} is real, symmetric ($V_{ij}=V_{ji}$) with elements

$$\begin{aligned} V_{11} &= V_0 - \frac{1}{7} \left[1 - 3 \frac{z^2}{r^2} \right] V_2 + \left[\frac{3}{28} - \frac{15}{14} \frac{z^2}{r^2} + \frac{5}{4} \frac{z^4}{r^4} \right] V_4, \\ V_{22} &= V_0 + \frac{1}{7} \left[1 - 3 \frac{z^2}{r^2} \right] V_2 \\ &\quad + \left[\frac{1}{56} - \frac{5}{28} \frac{z^2}{r^2} - \frac{5}{24} \frac{(x^2+6x^2y^2-y^4-z^4)}{r^4} \right] V_4, \\ V_{33} &= V_0 + \frac{1}{7} \left[1 - 3 \frac{z^2}{r^2} \right] V_2 \\ &\quad + \left[\frac{1}{56} - \frac{5}{28} \frac{z^2}{r^2} + \frac{5}{24} \frac{(x^4+6x^2y^2-y^4+z^4)}{r^4} \right] V_4, \\ V_{44} &= V_0 - \frac{1}{14} \left[1 - 3 \frac{(x^2-y^2-z^2)}{r^2} \right] V_2 \\ &\quad - \left[\frac{1}{14} - \frac{5}{42} \frac{(x^2-y^2-6z^2)}{r^2} + \frac{5}{6} \frac{z^2}{r^4} (x^2-y^2+z^2) \right] V_4, \\ V_{55} &= V_0 - \frac{1}{14} \left[1 + 3 \frac{(x^2-y^2-z^2)}{r^2} \right] V_2 \\ &\quad - \left[\frac{1}{14} + \frac{5}{42} \frac{(x^2-y^2-6z^2)}{r^2} - \frac{5}{6} \frac{z^2}{r^4} (x^2-y^2-z^2) \right] V_4, \\ V_{12} &= [(-x^2+y^2)/\sqrt{3} r^2] \left[\frac{3}{7} V_2 + \left(\frac{5}{28} - \frac{5}{4} \frac{z^2}{r^2} \right) V_4 \right], \\ V_{13} &= [xy/\sqrt{3} r^2] \left[-\frac{6}{7} V_2 - \left(\frac{5}{14} - \frac{5}{2} \frac{z^2}{r^2} \right) V_4 \right], \\ V_{14} &= [yz/\sqrt{3} r^2] \left[\frac{3}{7} V_2 - \left(\frac{15}{14} - \frac{5}{2} \frac{z^2}{r^2} \right) V_4 \right], \end{aligned}$$

$$V_{15} = [xz/\sqrt{3} r^2] \left[\frac{3}{7} V_2 - \left(\frac{15}{14} - \frac{5}{2} \frac{z^2}{r^2} \right) V_4 \right],$$

$$V_{23} = \frac{5}{6} \frac{xy(x^2 - y^2)}{r^4} V_4,$$

$$V_{24} = \frac{yz}{r^2} \left[-\frac{3}{7} V_2 - \left(\frac{5}{28} - \frac{15x^2 - 5y^2 + 5z^2}{12r^2} \right) V_4 \right],$$

$$V_{25} = \frac{xz}{r^2} \left[\frac{3}{7} V_2 + \left(\frac{5}{28} + \frac{5x^2 - 15y^2 - 5z^2}{12r^2} \right) V_4 \right],$$

$$V_{34} = \frac{xz}{r^2} \left[\frac{3}{7} V_2 + \left(\frac{5}{28} + \frac{-5x^2 + 15y^2 - 5z^2}{12r^2} \right) V_4 \right],$$

$$V_{35} = \frac{yz}{r^2} \left[\frac{3}{7} V_2 + \left(\frac{5}{28} + \frac{15x^2 - 5y^2 - 5z^2}{12r^2} \right) V_4 \right],$$

$$V_{45} = \frac{xy}{r^2} \left[\frac{3}{7} V_2 - \left(\frac{5}{21} - \frac{5z^2}{3r^2} \right) V_4 \right],$$

where $r^2 = x^2 + y^2 + z^2$ and V_0 , V_2 , and V_4 are the radial functions associated with the Legendre expansion in Eq. (2) of the text. These radial functions, are given for the case of O–Kr and O–Xe in Appendix B. The above given matrix elements are summed over all pairs and, subsequently, the interaction matrix is diagonalized to obtain eigenenergies and vectors.

APPENDIX B: RADIAL FUNCTIONS FOR Rg–O PAIR INTERACTIONS

For the ground state interactions, O(3P)–Rg, the isotropic and anisotropic radial functions given by the molecular beam scattering data are used as given.¹⁵ For the case of O(1D)–Kr, the radial functions are extracted from the *ab initio* data⁵ using Eq. (5) of the text, then fitted to the analytical forms:

$$V_0 = +M_{01} \exp[-M_{02}R] + M_0 \exp[-A(R - R_a)^2],$$

$$V_2 = -M_{21} \exp[-M_{22}(R - M_{23})^2] + M_2 \exp[-A(R - R_a)^2], \quad (\text{B1})$$

$$V_4 = -M_{41} \exp[-M_{42}(R - M_{43})^2] + M_4 \exp[-A(R - R_a)^2].$$

In the case of O–Xe, the second set of Gaussians in Eq. (B1), are not necessary to obtain fits within stated accuracies of the *ab initio* points. The dispersion term, in the form of Eq. (6) of the text is then added only to V_0 and V_2 . The fitted parameters are collected in Table II, and a comparison between the analytical pair interactions and the *ab initio* points is shown in Fig. 8.

For the isotropic O(1S)–Kr interaction, the same procedure as above is followed and a good fit is obtained as the sum of a single Gaussian and dispersion term [$C_6 = 24.78$ eV Å (Ref. 6)]. The fitted function that has been used, and is shown in Fig. 8, is

$$V[\text{O}(\text{}^1S)\text{-Kr}](R) = 100.94 \exp[-0.938(R + 0.00213)^2] - \zeta(R)C_6/R^6. \quad (\text{B2})$$

TABLE II. Pair potential parameters for O(1D)–Rg.

Parameter	Units	Kr	Xe
$C_6(V_0)$	eV Å ⁶	39.4	35.2
$C_6(V_2)$	eV Å ⁶	-8.74	-7.88
R_m	Å	3.75	3.9
M_{01}	eV	1135	1230
M_{02}	Å ⁻²	3.203	3.152
M_{21}	eV	32.20	16.53
M_{22}	Å ⁻²	1.040	1.149
M_{23}	Å	0.7393	1.224
M_{41}	eV	8.829	5.216
M_{42}	Å ⁻²	2.258	2.616
M_{43}	Å	1.056	1.374
M_0	eV	-0.025 39	
M_2	eV	-0.088 61	
M_4	eV	0.001 523	
A	Å ⁻²	1.031	
R_a	Å ⁻¹	2.79	
LC	Å	5.653	6.136

For the case of O(1S)–Xe, the experimentally determined gas phase potential of XeO($2^1\Sigma^+$) is used,²⁷ after fitting the given Rydberg–Klein–Rees (RKR) points to the sum of a Morse and a Gaussian:

$$V[\text{O}(\text{}^1S)\text{-Xe}](R) = 0.0838(\{1 - \exp[-2.62(R - 2.85)]\}^2 - 1) - 0.007 17 \exp[-(R - 4.02)^2/0.584]. \quad (\text{B3})$$

APPENDIX C: CAGE ANISOTROPY INDUCED TRANSITION DIPOLE

In the atomic basis set used, the $^1S \rightarrow ^1D$ transition is dipole forbidden. However, if we consider the central atom plus immediate nearest neighbors, then a dipolar charge distribution \mathbf{p} centered on the O atom is induced by the lattice fluctuations. The distribution is taken to be proportional to

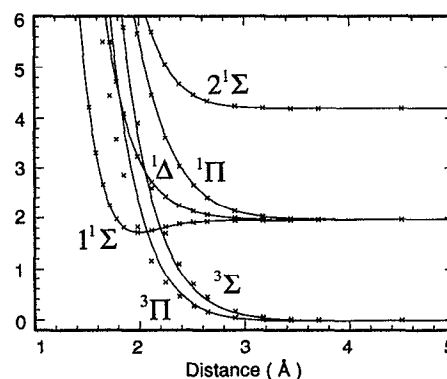


FIG. 8. Pair potentials of O–Kr. The solid lines are the fitted potentials used in the present treatment. The expressions and parameters are given in Appendix B. The crosses are the *ab initio* points (Ref. 5). In the case of the ground state, the solid lines are the potentials from scattering data (Ref. 14) which are used without further manipulations.

the first moment of the cage anisotropy, which is obtained by the vector sum of nearest neighbor atoms from the origin placed on atomic oxygen:

$$\mathbf{p} = \sum_{m=1}^{nn} q_m \mathbf{R}_m \propto \mathbf{r} = \sum_{m=1}^{nn} \mathbf{R}_m. \quad (\text{C1})$$

Including this induced term on the initial charge distribution of the 1S state, $Y_{0,0} + \gamma \mathbf{r}$, dipole induced transitions become allowed to the final state quadrupolar charge distribution given as $\sum_i \nu_{ij} |j\rangle$, in which $|j\rangle$ represent the five real D functions defined in Appendix A. The transition dipole $|\mu_{ij}|^2 = |\langle \varphi_j | e \mathbf{r} | \gamma \mathbf{r} \rangle|^2$ is most conveniently evaluated then by expanding \mathbf{r} in spherical harmonic basis. Explicitly,

$$\begin{aligned} |\mu_{ij}|^2 = & \gamma^2 \{ -a[(\nu_{j1}/\sqrt{3}) - \nu_{j2} + \nu_{j3} - \nu_{j5}] \\ & -b[(\nu_{j1}/\sqrt{3}) + \nu_{j2} + \nu_{j3} + \nu_{j4}] \\ & +c[2(\nu_{j1}/\sqrt{3}) - \nu_{j4} + \nu_{j5}] \}^2, \end{aligned} \quad (\text{C2})$$

where a , b , and c , are the x , y , and z components of the anisotropy vector, and ν_{ji} are the components of eigenvector associated with eigenstate J of the lower state.

¹A. V. Danilychev and V. A. Apkarian, *J. Chem. Phys.* **99**, 8617 (1993).

²H. Krueger and E. Weitz, *J. Chem. Phys.* **96**, 2846 (1992); E. T. Ryan and E. Weitz, *J. Chem. Phys.* **99**, 8628 (1993).

³H. Kunttu, J. Feld, R. Alimi, and V. A. Apkarian, *J. Chem. Phys.* **92**, 4856 (1990).

⁴R. Alimi, R. B. Gerber, and V. A. Apkarian, *J. Chem. Phys.* **92**, 3551 (1990).

⁵T. H. Dunning, Jr. and P. J. Hay, *J. Chem. Phys.* **66**, 3767 (1977); *J. Chem. Phys.* **74**, 3718 (1981).

⁶W. G. Lawrence and V. A. Apkarian, *J. Chem. Phys.* **97**, 6199 (1992).

⁷W. G. Lawrence and V. A. Apkarian (unpublished).

⁸J. A. Boatz and M. E. Fajardo (unpublished).

⁹See, for example, W. E. Baylis, *J. Phys. B* **10**, L477 (1977).

¹⁰The angularly anisotropic open shell-closed shell interaction potentials have been treated rigorously in treatments of gas phase scattering experiments, the classical work deals with alkali atom plus rare gas collisions: E. E. Nikitin, *J. Chem. Phys.* **43**, 744 (1965); W. E. Baylis, *J. Chem. Phys.* **51**, 2665 (1969); R. H. G. Reid and A. Delgarno, *Phys. Rev. Lett.* **22**, 1029 (1969); and halogen + H^+ collisions: F. H. Mies, *Phys. Rev. A* **7**, 942 (1973); **7**, 957 (1973).

¹¹D. Maillard, J. Fournier, H. H. Mohammed, and C. Girardet, *J. Chem. Phys.* **78**, 5480 (1983).

¹²L. C. Balling and J. J. Wright, *J. Chem. Phys.* **79**, 2941 (1983).

¹³V. Aquilanti and G. Grossi, *J. Chem. Phys.* **73**, 1165 (1980).

¹⁴V. Aquilanti, R. Candori, and F. Pirani, *J. Chem. Phys.* **89**, 6157 (1988).

¹⁵J. S. Cohen, W. R. Wadt, and P. J. Hay, *J. Chem. Phys.* **71**, 2955 (1979).

¹⁶P. S. Julienne and M. Krauss, *J. Mol. Spec.* **56**, 270 (1975).

¹⁷J. A. Barker, R. A. Fisher, and R. O. Watts, *Mol. Phys.* **21**, 657 (1971).

¹⁸See, for example, W. H. Flygare, *Molecular Structure and Dynamics* (Prentice Hall, Englewood Cliffs, NJ, 1978).

¹⁹S. R. Langhoff, *J. Chem. Phys.* **73**, 2379 (1980).

²⁰R. Kubo and Y. Toyozawa, *Prog. Theor. Phys.* **13**, 160 (1955).

²¹M. Lax, *J. Chem. Phys.* **20**, 1752 (1952).

²²E. A. Gislason, *J. Chem. Phys.* **58**, 3702 (1973); E. J. Heller, *J. Chem. Phys.* **68**, 2066 (1978).

²³N. Metropolis, A. W. Rosenbluth, M. N. Rosenbluth, A. H. Teller, and E. Teller, *J. Chem. Phys.* **21**, 1087 (1953).

²⁴W. G. Lawrence and V. A. Apkarian, *J. Chem. Phys.* **97**, 2224 (1992).

²⁵I. H. Gersonde and H. Gabriel, *J. Chem. Phys.* **98**, 2094 (1993).

²⁶I. Last and T. F. George, *J. Chem. Phys.* **87**, 1163 (1987); I. Last, T. F. George, M. E. Fajardo, and V. A. Apkarian, *J. Chem. Phys.* **87**, 5917 (1987).

²⁷J. D. Simons, A. G. Maki, and J. T. Hougen, *J. Mol. Spec.* **74**, 70 (1979).